Determining Peptide Sequence Effects That Control the Size, Structure, and Function of Nanoparticles

Ryan Coppage,[†] Joseph M. Slocik,[‡] Beverly D. Briggs,[†] Anatoly I. Frenkel,[§,*] Rajesh R. Naik,[‡,*] and Marc R. Knecht[†,*]

[†]Department of Chemistry, University of Miami, 1301 Memorial Drive, Coral Gables, Florida 33146, United States, [‡]Nanostructured and Biological Materials Branch, Air Force Research Laboratory, Wright-Patterson Air Force Base, Ohio 45433-7702, United States, and [§]Department of Physics, Yeshiva University, 245 Lexington Avenue, New York, New York 10016, United States

ABSTRACT

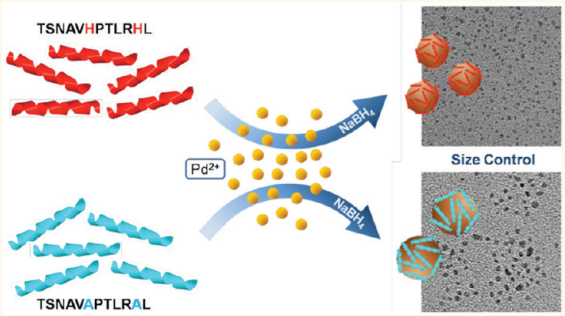

The ability to tune the size, shape, and composition of nanomaterials at length scales <10 nm remains a challenging task. Such capabilities are required to fully realize the application of nanotechnology for catalysis, energy storage, and biomedical technologies. Conversely, nature employs biomacromolecules such as proteins and peptides as highly specific nanoparticle ligands that demonstrate exacting precision over the particle morphology through controlling the biotic/abiotic interface. Here we demonstrate the ability to finely tune the size, surface structure, and functionality of single-crystal Pd nanoparticles between 2 and 3 nm using materials directing peptides. This was achieved by selectively altering the peptide sequence to change the binding motif, which in turn modifies the surface structure of the particles. The materials were fully characterized before and after reduction using atomically resolved spectroscopic and microscopic analyses, which indicated that the coordination environment prior to reduction significantly affects the structure of the final nanoparticles. Additionally, changes to the particle surface structure, as a function of peptide sequence, can allow for chloride ion coordination that alters the catalytic abilities of the materials for the C—C coupling Stille reaction. These results suggest that peptide-based approaches may be able to achieve control over the structure/function relationship of nanomaterials where the peptide sequence could be used to selectivity tune such capabilities.

KEYWORDS: bionanotechnology · peptide · biomimetic · catalysis · Pd nanoparticle

Nature has evolved varied approaches to fabricate complex inorganic architectures composed of nanoscale building blocks, all of which are mediated at the molecular level.[1−4] Control over these processes is achieved through peptide and protein chemical interactions with the inorganic component for defensive, structural, and bioremediation functions at ambient conditions, contrasting with the conditions traditionally employed for materials synthesis.[2] By mimicking biological processes, translation of desirable ambient methods toward fabrication routes for nonbiological materials could be achieved to advance current technological applications. This has been addressed by the virus and peptide-based fabrication of batteries,[5,6] catalysts,[7−13] sensors,[14,15] and complex nanoparticle assemblies.[16−19] While biological approaches represent new avenues to realize next-generation materials, a fundamental understanding of the structure/function relationship of the peptide/inorganic surface is required, where minor modifications could be used to fine-tune the structure, shape, composition, and functionality of the final materials.

Accessing an atomically resolved image of the peptide conformation on the surface of nanoparticles remains a significant challenge. While biocombinatorial approaches have isolated numerous peptides with affinities for different inorganic compositions,[20] such methods provide little information concerning how the peptides interact at the molecular level for materials specificity. Additionally, these approaches are likely to isolate sequences with the greatest affinity for the target; however, such sequences may not be optimal for the intended functionality/application of the material. It is likely that select amino acid residues and the peptide secondary structure work in combination to control the binding, stability, and final activity of the nanoparticle. By accessing such information, new sequences could be rationally designed that can direct the fabrication of materials with control over the structure, composition, and functionality. Computational models are available that probe peptide binding of target 2D flat surfaces;[21−23] however, modeling studies of binding to 3D dispersed materials in an aqueous environment remain limited.[24] While these analyses are

* Address correspondence to knecht@miami.edu, rajesh.naik@wpafb.af.mil, anatoly.frenkel@yu.edu.

Received for review November 26, 2011 and accepted January 25, 2012.

Published online January 25, 2012
10.1021/nn204600d

© 2012 American Chemical Society

integral to understanding the bio/nano surface, experimental evidence is required to refine this structural level. Unfortunately, only a handful of experimental methods are available to achieve these goals, where the limit of resolution complicates such analyses.

We have used computational modeling of peptide binding as a foundation for the development of experimental approaches to probe the peptide/inorganic interface.[9−11,22] Using phage display, the Pd4 peptide (TSNAVHPTLRHL) was isolated with affinity for Pd.[11] Pandey *et al.* have employed Monte Carlo modeling of Pd4 binding to a 2D surface, which indicated that the histidines at the 6 and 11 positions anchor to Pd to create a kinked-loop structure.[22] Upon the basis of these theoretical results, a series of four peptides, listed in Table 1, were synthetically prepared that modified peptide binding at these selected sites.[10] To that end, the A6, A11, and A6,11 peptides were prepared that swapped histidine with alanine at the 6, 11, and 6 and 11 positions, respectively. This resulted in the removal of binding at these locations to alter the peptide conformation once bound to a Pd nanoparticle.[10] Interestingly, the Pd nanoparticles fabricated using these different sequences are highly catalytically active for Stille C−C coupling and suggest that the bio/nano surface plays a role in controlling the reactivity. The structure and the functionality of the materials are anticipated to arise from the strict interactions of the peptide on the nanoparticle surface, which is likely embedded during the peptide isolation process for the parent sequence. Such interactions are potentially modulated based upon changes to the peptide sequence that are reflected in the functionality. Furthermore, the peptides could play a significant role throughout nanoparticle synthesis. In this regard, the Pd^{2+} ions bind the peptide to form Pd^{2+}/peptide complexes that could contribute to the structure of the final materials. These complexes are anticipated to change based upon the peptide sequence, which controls the binding stoichiometry and motifs, as well as through the number of Pd^{2+} ions bound to the peptide. Such interactions could alter the structure of the zerovalent materials fabricated upon reduction where minimal understanding of the interplay between peptide sequence, metal ion complexes, and the final materials is known.

In this contribution, we demonstrate that changes in the particle size and functionality can be directly achieved *via* minor variations in the materials-directing peptide sequence. This was achieved by a complete experimental analysis of the fabrication and catalytic activity of Pd nanoparticles using the peptide library of Table 1 from Pd^{2+}/peptide complexation prior to reduction to the final Pd^0 nanoparticles. By using UV−vis and X-ray absorbance analyses of the loading of Pd^{2+} in the reaction mixture, monitoring of metal/peptide complexation can be achieved to determine

TABLE 1. Peptide Library Used To Prepare Pd Nanoparticles

			Pd/peptide ratio size(nm)			
peptide	sequence	pI[a]	1	2	3	4
Pd4	TSNAVHPTLRHL	9.47	1.9 ± 0.3	1.9 ± 0.3	2.1 ± 0.4	2.0 ± 0.3
A6	TSNAVAPTLRHL	9.44	2.4 ± 0.6	2.1 ± 0.5	2.2 ± 0.7	2.1 ± 0.4
A11	TSNAVHPTLRAL	9.44	2.3 ± 0.4	2.4 ± 0.5	2.6 ± 0.4	2.4 ± 0.5
A6,11	TSNAVAPTLRAL	9.41	2.8 ± 0.7	3.0 ± 0.6	2.8 ± 0.7	3.1 ± 0.7

the maximum Pd/peptide ratios that can be used for materials synthesis as a function of the peptide sequence. We also observe the formation of different peptide secondary structures based upon the peptide sequence and number of Pd^{2+} ions per peptide, which has implications on nanoparticle formation. Upon reduction, the fabrication of single-crystal Pd nanoparticles occurs where fine-tuning of the particle size is achievable based on the peptide sequence. For instance, minor modifications that replace only a single amino acid residue can have observable changes on the particle morphology. Furthermore, the sequence position of the modifications to the peptide is also critically important in controlling the structure/function relationship of the final particle. To that end, modifications at the 11 position result in larger particles with diminished catalytic functionalities, while variation at the 6 position produces smaller particles that possess the highest degree of activity. This change in activity is attributed to the surface structure of the materials, which is directly tuned by the peptides at the biotic/abiotic interface. This analysis is important for three key reasons. First, it demonstrates a high level of structural/size control over nearly monodisperse, single-crystal nanoparticles at significantly small sizes by simple changes to the materials directing sequence; such control remains challenging using standard ligand-based nanoparticle synthetic approaches. Second, the morphology of the metal ion/peptide complex prior to reduction is shown to be important to the final structure and function of the materials as a result of the degree of metal ion complexation. Third, the results present key peptide sequence effects information, which could be used in the foundation of principles for the *de novo* design of materials-directing peptides that control the structure/function relationship of nanomaterials.

RESULTS AND DISCUSSION

The Pd4 peptide was identified by phage display with affinity for Pd where recent results suggest that the sequence binds to crystallographic features to produce Pd nanoparticles of ∼2 nm.[9,11] These materials are catalytically active under desirable environmentally friendly and energy neutral conditions; however, the biotic/abiotic interface of these structures plays a

significant role in mediating the reactivity.[10] While it is clear that the peptide participates in the functionality, it remains unclear as to the mechanism by which the sequence controls the structure of the materials. The material structure, which encompasses size, shape, and composition, is critically important to the overall reactivity where all three characteristics can be individually modified to have dramatic implications on the final activity. Ideally, these traits could be controlled simultaneously by using the selected ligands; however, such ligands must be sufficiently complex to allow for this level of structural control. Peptides are optimal choices for this capability due to their facile synthesis and sequence programmability, as well as the diverse range of binding moieties and arrangements achievable by peptide secondary structure. To probe this materials' synthetic capabilities, a set of three analogue peptides of the parent Pd4 sequence were studied that modified the binding motif at the histidine residues to result in the A6, A11, and A6,11 peptides.

An important key factor in materials structural control lies in the metal/ligand complex prior to reduction. To determine the potential number of Pd^{2+} binding sites for each of the four sequences, titration of a peptide solution with K_2PdCl_4 was employed, which was monitored using UV−vis spectroscopy. This was achieved by monitoring the ligand-to-metal charge transfer band (LMCT) that is observed at 215 nm, which is present for the binding of Pd^{2+} by the amines of the individual peptides.[11,27] As a control, Figure 1a presents this analysis for the K_2PdCl_4 precursor in solution in the absence of peptide. Here, two absorbance peaks are observed at 207 and 235 nm that arise from the uncomplexed Pd^{2+} salt, whose absorbance values are dependent upon the concentration. Note that the Pd^{2+} concentrations presented are those that are employed to prepare Pd/peptide ratios between 1 and 10 in the materials synthesis reactions, thus a direct comparison can be drawn to the control study. Additionally, no peaks are evident at the two lowest Pd^{2+} concentrations due to the molar absorptivity of the metal salt. As presented in Figure 1b, again in the absence of peptide, the 207 and 235 nm absorbance intensities increase linearly with the Pd^{2+} concentration as anticipated by Beer's Law.[28]

Figure 1c presents the UV−vis analysis of the Pd^{2+} complexation reaction with the Pd4 peptide. In this study, the peptide concentration remained constant while the Pd^{2+} concentration varied at the values shown in Figure 1a, to result in Pd/peptide ratios of 1−10. While the peptides alone demonstrated minimal to no absorbance over the wavelength range of interest (Supporting Information, Figure S1), all UV−vis analyses of the Pd^{2+}/peptide complexes and peptide-capped Pd^0 nanoparticles were background-subtracted against the free peptide at the reaction concentration. The black spectrum displays the reaction at a ratio of 1 where a single peak is observed at 215 nm that arises from the LMCT band of Pd^{2+}/amine binding. Note that, in the absence of the peptide, no absorbance is noted for the Pd^{2+} species in solution (black spectrum, Figure 1a). As the Pd/peptide ratio is increased to 2 (red spectrum), the LMCT band intensity increases with no additional peaks being noted. This increasing trend is maintained for ratios up to 4 (blue spectrum); however, a peak shoulder is observed at 235 nm at this ratio, consistent with free Pd^{2+} in solution. At subsequently higher ratios ($\geq$5), the 215 nm LMCT band begins to shift to 207 nm and the 235 nm peak increases in intensity, suggesting that the peptide becomes saturated with Pd^{2+} binding and excess metal salt remains uncoordinated and free in solution.

The plot of the growth of the three peaks associated with peptide metal binding is presented in Figure 1d. While a linear trend in absorbance growth is observed for the free Pd^{2+} salt in solution, a deviated trend is noted for the reaction in the presence of the Pd4 peptide. In this system, the LMCT growth associated with peptide binding induces the 215 nm band to rapidly increase in absorbance at low Pd/peptide ratios. The derivative of the trend line for the 215 nm plot as a function of Pd/peptide ratio demonstrates an inflection point at 5.5. This suggests that, at values greater than this ratio, additional Pd^{2+} ions remain in solution unbound by the peptide. Similar observations are noted with the 207 nm absorbance, which is likely due to the broad absorptivity of the LMCT band. This also explains why only a minimal deviation is observed for the 235 nm absorbance as it is sufficiently positioned to avoid significant signal overlap. Nevertheless, these changes in the linear absorbance trend are rooted in the binding of Pd^{2+} to the peptide amines. From this, it can be estimated that ~5 or less Pd^{2+} ions can coordinate to the peptide as the deviated trend is maintained at these values. At higher ratios, the slope of the trend lines for the 207 and 235 nm absorbance of the Pd^{2+} returns to those of the peptide-free solution, thus suggesting uncoordinated metal salt exists in the reaction mixture.

Figure 1e−g presents the trend analysis of Pd^{2+} complexation with the A6, A11, and A6,11 peptides, where the actual absorbance spectra are presented in the Supporting Information, Figure S2. Interestingly, for the A6 and A11 titration studies, presented in Figure 1e and f, respectively, a similar trend to the Pd4 peptide is observed. For both samples, inflection points are noted at a Pd/peptide ratio of 4, suggesting that these samples can coordinate slightly less Pd^{2+} ions compared to the parent sequence. This was not surprising as a metal coordination site at the substituted histidine residue was removed. Changes in the absolute intensities for the different samples likely arise from different coordination environments (confirmed *via* Circular Dichroism (CD) spectroscopy, discussed

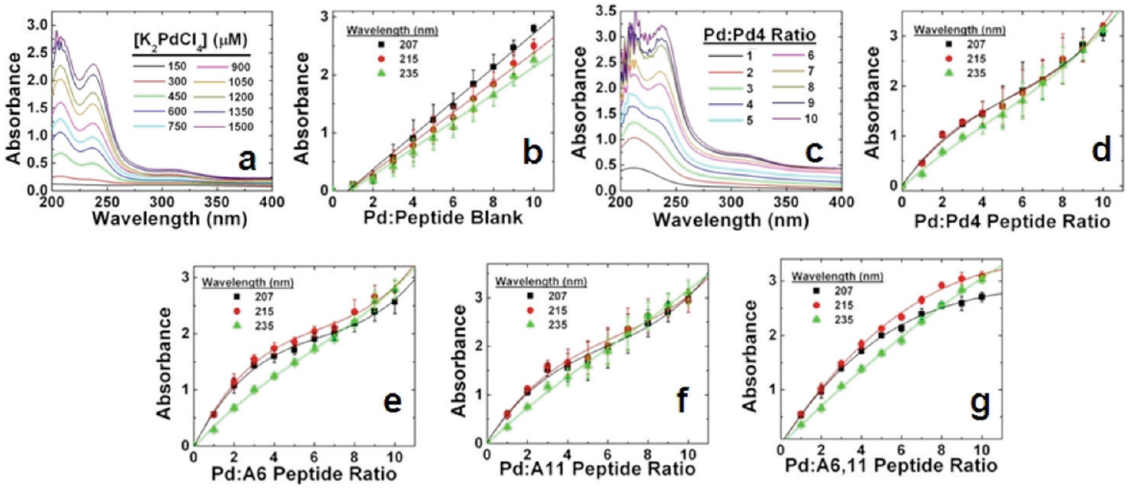

Figure 1. UV−vis analysis of the K_2PdCl_4 titration. (a) UV−vis spectra of the Pd^{2+} salt in the absence of peptide and (b) absorbance trend as a function of concentration. (c) UV−vis spectra of the formation of the Pd^{2+}/peptide complex using the Pd4 peptide, where the absorbance trend as a function of Pd^{2+}/peptide ratio is presented in (d). The absorbance trends are also presented for the peptide analogues: (e) A6, (f) A11, and (g) A6,11.

below) and sample blanks (based upon the different sequences). For the A6,11 peptide that removes both histidine residues, as shown in Figure 1g, a significantly deviated trend is observed as compared to the Pd4, A6, and A11 systems. In this system, saturation of the Pd^{2+} binding to the peptide is not spectroscopically observed at Pd/peptide ratios ≤10. Taken together, this suggests that the histidine, arginine, and asparagine residues, as well as the N-terminus and peptide backbone, likely play a significant role in metal ion complexation prior to reduction. Furthermore, the A6,11 peptide has a significantly different solution structure (discussed below), as compared to the other three sequences, which suggests that peptide conformation could lead to binding site exposure that may be involved in metal ion complexation.

After peptide complexation by the metal ions, reduction is required to drive nanoparticle nucleation and growth. As shown in the Supporting Information, Figure S3 presents images of the reactions after addition of a 10-fold excess of $NaBH_4$ to the mixtures with different Pd/peptide ratios of ≤7 for the four peptides. For all of the materials prepared using the Pd4, A6, and A11 peptides, stable nanoparticles are generated at ratios ≤4; however, at greater ratios, precipitation of bulk Pd black is observed. This correlates very well with the titration experiments that indicated metal ion saturation of the peptides at a ratio of 4. Similar results were noted for the Pd nanoparticles prepared using the A6,11 sequence; however, stable nanoparticles were generated up to a ratio of 5. Precipitation of bulk Pd was not noted until ratios ≥6. Due to this precipitation event, only those materials that formed stable colloidal solutions were further analyzed.

Initial characterization of the reduced materials was conducted by UV−vis spectroscopy and high-resolution Transmission Electron Microscopy (TEM) analysis. Figure 2 presents the UV−vis spectra of the

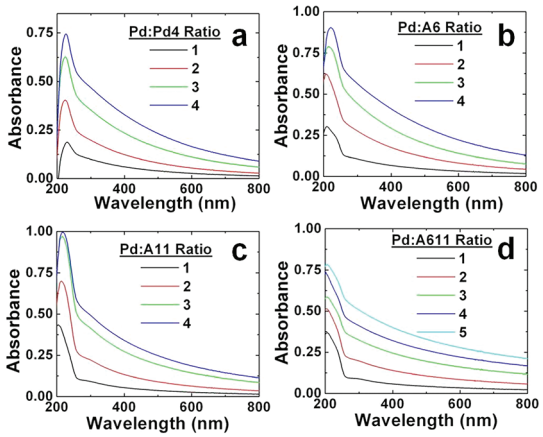

Figure 2. UV−vis analysis of reduced Pd nanoparticles prepared at the selected Pd/peptide ratios employing the (a) Pd4, (b) A6, (c) A11, and (d) A6,11 peptide.

materials prepared at the different ratios that generated stable nanoparticles for the four different peptides. Figure 2a specifically represents the analysis for the Pd4-based materials at ratios ≤4. Here, for all four samples, an increase in absorbance toward lower wavelengths was noted, while the LMCT band and the absorbances associated with Pd^{2+} were not observed, all of which is consistent with Pd nanoparticle formation. Additionally, the intensity of the absorbance at all wavelengths increased as the Pd/peptide ratio increased such that the materials prepared at a ratio of 4 possessed the highest intensity. Identical results were observed for all materials prepared with the different peptides (Figure 2b−d for the A6, A11, and A6,11-based materials, respectively) such that no absorbance bands are observed for unreduced Pd^{2+} and that the absorbance intensity increases proportional to the Pd/peptide ratio. This suggests that Pd nanoparticles are prepared under the selected

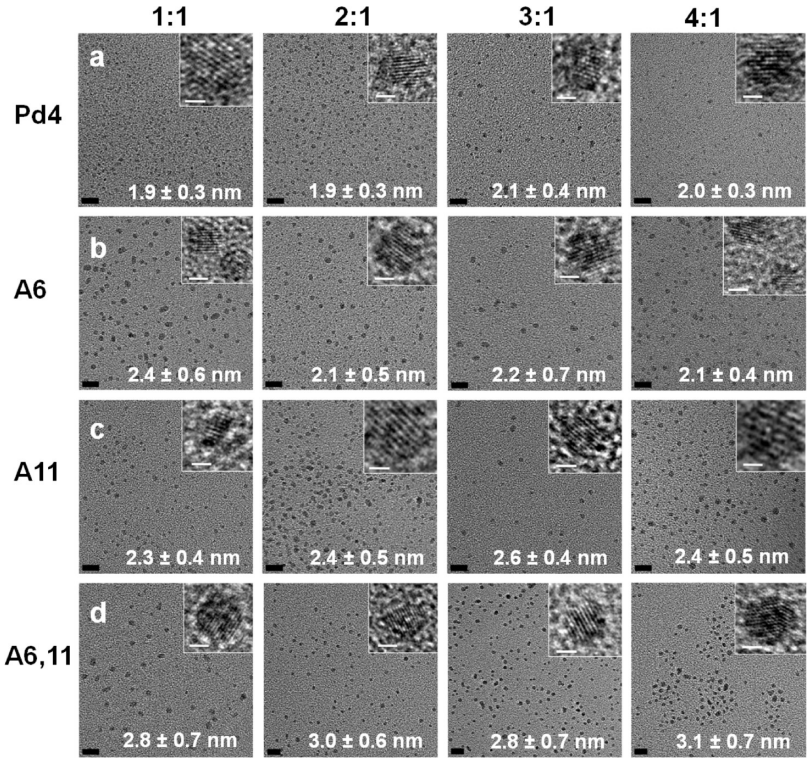

Figure 3. TEM analysis of the materials generated at the indicated Pd/peptide ratios in the presence of the (a) Pd4, (b) A6, (c) A11, and (d) A6,11 peptide. The inset displays a high-resolution image of the nanoparticles demonstrating characteristic (111) lattice fringes of fcc Pd. The black scale bars represent 10 nm, and the inset white scale bars represent 2 nm.

conditions; however, UV−vis is not able to discern changes in the Pd nanoparticle structure. To further probe the material morphology on the nanoscale, TEM analysis was conducted.

TEM studies of the Pd4-capped Pd nanoparticles are presented in Figure 3a, with a high-resolution image of an individual particle displayed in the insets. Here, single-crystal Pd nanoparticles with an average size of 1.9−2.1 nm are prepared regardless of the Pd/peptide ratio used during synthesis. Specifically, particle sizes of 1.9 ± 0.3, 1.9 ± 0.3, 2.1 ± 0.4, and 2.0 ± 0.3 nm were achieved for materials prepared at ratios of 1, 2, 3, and 4, respectively, which is consistent with previous studies.[9] When the materials prepared with the A6 peptide were analyzed (Figure 3b), again single-crystal Pd materials were generated; however, the average particle size shifted to between 2.1 and 2.4 nm. Furthermore, a narrow size distribution was achieved for these materials, especially for particles of such small sizes. Analysis of the A11-based particles, as presented in Figure 3c, indicated a further shift to slightly larger particles with average sizes between 2.3 and 2.6 nm that were again single-crystal nanomaterials. Finally, the nanoparticles prepared with the A6,11 peptide (Figure 3d), which modifies both anchor residues to remove binding at these sites, demonstrated the largest particles with average sizes between 2.8 and 3.1 nm. As listed in Table 1 and seen in Figure S2 of the Supporting Information, trends in the particle size as a function of peptide sequence and Pd/peptide ratio can be generalized. First, it is noted that, regardless of the Pd/peptide ratio employed to prepare the materials, particles of approximately the same size and distribution are generated when using the same peptide. Second, a general trend of increasing average particle size is observed as a function of the capping peptide sequence (Pd4 < A6 < A11 < A6,11). Interestingly, for all materials that are produced, regardless of the nanoparticle size, Pd/peptide ratio, and passivating sequence, single-crystal nanoparticles are obtained, which can be difficult to achieve for Pd particles of <5 nm.

To elucidate this unique structural trend, further spectroscopic analysis of the materials before and after reduction was conducted. CD spectra of the peptide library showed similar trends upon coordination of Pd^{2+} ions and nanoparticle formation. Collectively, all of the peptides became increasingly more unordered at higher Pd^{2+}/peptide ratios as shown by a loss in ellipticity due to Pd^{2+} coordination at multiple peptide binding sites present within the different peptides (Figure 4). In general, as the ratio of Pd^{2+}/peptide was increased, the negative CD band at 203 nm ($n \rightarrow \pi^*$) decreased in intensity and shifted to longer wavelengths, while a new CD peak was generated at ~250 nm for the uncomplexed Pd^{2+} salt. Alternatively, upon reduction of Pd^{2+} ions to Pd^0 nanoparticles, the corresponding peptides partially regained some

secondary structure in order to accommodate nanoparticle binding but, moreover, were independent of the Pd/peptide ratio (Figure 4). In total, deconvolution of the peptide CD spectra into individual secondary structure components using CDPro (helix, 3_{10} helix, strand, turn, polyproline type II helix, and unordered) revealed that the free and nanoparticle-bound peptides were predominantly unordered (~45%) with low helical content (~6%) (Supporting Information, Table S2). Notably, these structural features remained largely unchanged upon nanoparticle binding as depicted by a flat line when plotted against the different peptide/nanoparticle ratios. However, the amount of turn and strand motifs contributing to the overall peptide secondary structure were substantially affected by nanoparticle binding for the peptide set. By comparison, the Pd4 and A11 peptides exhibited the largest structural changes, while the A6,11 peptide remained mostly unaltered on the nanoparticle surface relative to its free conformation in solution. This suggests that the A6,11 peptide minimally interacts with the Pd nanoparticle through possibly only the N-terminus amine, thereby favoring the synthesis of larger sized particles as confirmed above. In contrast, the altered CD structure of the parent Pd4 showed an increased percentage of turns and decreased number of strands in the presence of Pd metal. This suggests a strong peptide/nanoparticle interaction, which invariably affects the resulting nanoparticle size and is consistent with a peptide structure that is constrained at multiple sequence sites along the nanoparticle surface. Conversely, for the pair of peptides with single alanine substitutions (A6 and A11), an increased percent of strands and decreased number of turns were observed after nanoparticle formation, although at lesser extents for A6. In the case of the nanoparticles capped with the A11 peptide, the number of turn structural motifs decreased from 24 (free) to 6% (bound), while the strand content increased from 0 to ~32%. Similarly, the A6 peptide showed a 6% decrease in turn content and an increase of 21% for the strand component. In these cases, the peptides are less constrained along the nanoparticle and can adopt a strand motif extended from the surface. This difference in stabilization is consistent with peptide adsorption measurements obtained through a Quartz Crystal Microbalance (QCM) analysis, as shown in the Supporting Information, Figure S5. By QCM, the A6,11 peptide showed the lowest binding affinity to a Pd-coated crystal, while the A6 peptide had the largest affinity. Also, both the A11 and A6,11 showed more desorption from the surface and loss of mass as compared to Pd4 and A6, which remained tightly bound. These results confirm that the location of the alanine substitution is critical in defining the peptide structure on the nanoparticle surface and in modulating the catalytic activity (discussed below).

To more fully characterize the materials, both the prereduced Pd^{2+}/peptide complexes and the zerovalent Pd nanoparticles, X-ray absorption fine structure (XAFS) spectroscopy was performed. Experimental extended XAFS (EXAFS) spectra and best theoretical fits are shown in Supporting Information, Figure S6. The nearest neighbor coordination numbers (CNs) were obtained for all three types of Pd neighbors: O/N, Cl, and Pd atoms in the sample. Note that these values are averaged over all Pd atoms in the sample that absorbed X-rays, thus such values are representative of the entire ensemble, not a specific nanoparticle or a complex. Figures 5a and b present the Pd−O/N and Pd−Cl first nearest neighbor CN values for the Pd^{2+}/peptide complexes prior to reduction. Since EXAFS is incapable of distinguishing between O and N scatterers due to their similar *Z*-numbers, these values are reported as O/N. As shown in Figure 5a for the Pd−O/N CNs, it is clear that a trend of decreasing O/N coordination occurs as the Pd^{2+}/peptide ratio is increased from 1 to 4. Conversely, as shown in Figure 5b, the Pd−Cl CNs are shown to be directly proportional to the Pd^{2+}/peptide ratio such that they linearly increase over the ratios that are studied. This suggests that, at low ratios, the Pd^{2+} ions possess more coordination with O/N from the peptide over Cl ions, while at higher ratios, more Cl coordination is present to the metal ions as compared to O/N. Furthermore, for each peptide at each ratio, the sum of the Pd−O/N CN and Pd−Cl CN equals 4, within the experimental uncertainties, which fits exactly with the number of ligands anticipated for the Pd^{2+} ions. Taken together, the data demonstrate increased peptide coordination for the Pd^{2+} ions at low ratios that decreases at higher ratios. At the higher ratios, increased Cl^- coordination to the Pd^{2+} ions is required to reach a four-coordinate system. Furthermore, at the higher ratios, free Pd^{2+} species may be in solution, which would also account for the additional Pd−Cl coordination observed. This EXAFS data confirm the coordination of the peptide to the Pd^{2+} ions in solution to form the Pd^{2+}:peptide complex regardless of the peptide sequence, which plays a role in the reduction of the materials.

EXAFS analysis of the CN values for the peptide-capped zerovalent Pd nanoparticles is presented in Figure 5c−e. Specifically, Figure 5c presents the Pd−Pd nearest neighbor CNs for all four peptide-based systems. From the Pd−Pd CN, critically important information concerning the nanoparticle structure can be achieved in combination with TEM results. As shown previously,[9] for the Pd4-based materials, as the Pd/peptide ratio for the sample increases, a proportional increase in the Pd−Pd CN is observed (red plot). This trend can be attributed to either the increasing particle size[29] or the increasing degree of Pd^{2+} reduction in the sample, or both. Since the average particle size remains constant, as per TEM observations, the decreased CN

values for the lower ratios can be explained solely on the degree of reduction that is lower in these systems. The degree of reduction is directly related to the coordination complex generated prior to reduction where more coordination to the peptide could shift the reduction potential, thus making the materials more difficult to reduce.[9] Indeed, EXAFS analysis of the prereduced complex demonstrates increased peptide coordination to the Pd^{2+} metal ions, further supporting this hypothesis. Analysis of the CN values for the Pd nanoparticle prepared with the A6 peptides demonstrates a substantially different trend as a function of the Pd/peptide ratio as compared to the Pd4 system. Here, regardless of the ratio, nearly identical Pd−Pd CNs of ∼6 are observed. This value is smaller than the theoretical value of 9.84 (assuming a perfect cuboctahedron) for particles of ∼2.2 nm in diameter,[29] as observed by TEM. This suggests that partial reduction of the Pd^{2+} in the sample occurs, similar to the Pd4 sample; however, the coordination environment plays a less significant role in this process as equivalent degrees of reduction are present at all four Pd/peptide ratio samples. This equivalent degree of reduction is inferred from the identical particle size that is observed for the sample by TEM. Furthermore, a higher degree of reduction for all samples is evident when using the A6 peptide as compared to the parent Pd4 sequence.

Analysis of the Pd−Pd CN for the A11-based structure is presented in the royal blue plot of Figure 5c. Here, highly varied values are observed, which are likely due to the statistical noise of the EXAFS analysis. In this system, CNs of 3.3, 4.9, 3.3, and 4.2 are noted at Pd/peptide ratios of 1, 2, 3, and 4, respectively. Overall, these values are small, compared to the A6-capped particles, suggesting a lower degree of reduction. Finally, the Pd−Pd CN values for the A6,11-based materials are shown in the light blue data of Figure 5c. For these materials, high CNs of ∼6 are noted that are similar to the A6-prepared nanoparticles at all of the Pd/peptide ratios studied. Note that these materials are ∼1 nm in diameter larger than the A6-capped structures, thus a larger Pd−Pd CN value would

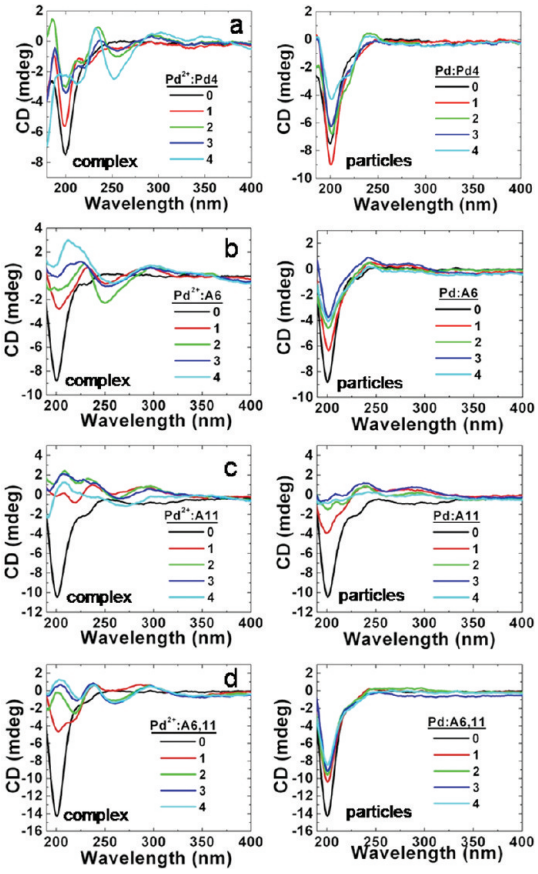

Figure 4. CD analysis of the peptide titration in the presence of the (a) Pd4, (b) A6, (c) A11, and (d) A6,11 peptides. The graph on the left presents the unreduced Pd^{2+}/peptide complexes, while the figure on the right presents the analysis of the reduced nanoparticles.

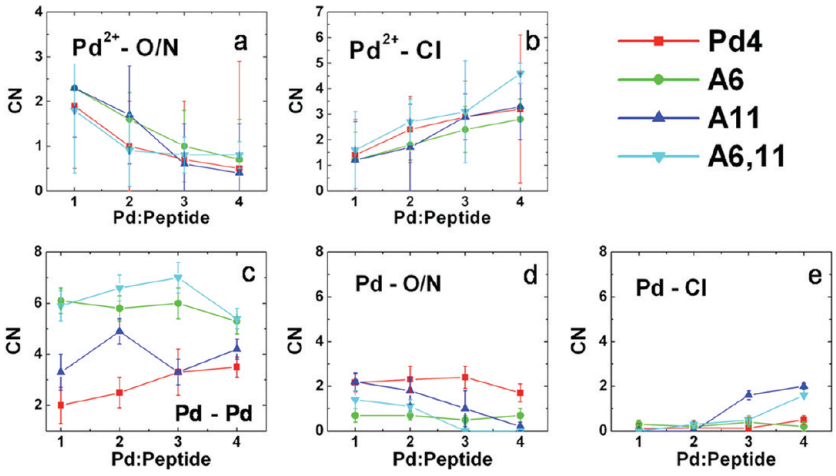

Figure 5. EXAFS-based CN trend analysis. (a and b) Pd^{2+}−O/N and Pd^{2+}−Cl CN trend for the unreduced Pd^{2+}/peptide complexes, respectively. (c) Trend analysis for the Pd−Pd CN values for the reduced nanoparticles, and (d and e) Pd−O/N and Pd−Cl CN trend plots for the reduced materials, respectively.

be expected of A6,11 with more internal Pd atoms increasing the CN average.[29] This increase is observed over the value range of 5.4–6.8 for the Pd–Pd CN, though lower than a particle that size should ideally possess. This suggests that a slightly smaller fraction of Pd^{2+} is reduced in the A6,11 sample to result in the observed CN values as compared to the A6 materials. Taken together, this difference in the reduction for all of the different peptide-based samples evident in the Pd–Pd CN was surprising; however, the peptide secondary structure and binding of the Pd^{2+} ions may facilitate this capability.

Analysis of the Pd–O/N and Pd–Cl CNs for the reduced nanoparticles with the four different peptide ligands is presented in Figures 5d and e, respectively. For the Pd4- and A6-capped materials, nearly equivalent Pd–O/N CN values for the two systems are observed across the selected Pd/peptide ratios used during materials synthesis; however, for the A11- and A6,11-prepared Pd nanoparticles, a linear decrease in O/N coordination to Pd is noted as the ratio employed to fabricate the materials increases. Concurrent with this particle surface environment, the Cl coordination to the Pd materials is different as selected for by the peptide used to generate the particles. For instance, using the parent Pd4 and A6 sequences, minimal to no Cl is present within the first coordination sphere of the Pd nanoparticle on average in the samples. Interestingly, for the A11- and A6,11-capped particles, Cl coordination is evident for the materials generated at the higher Pd/peptide ratios. For both systems, no Cl is present when the materials are produced at Pd/peptide ratios of ≤ 2; however, the Pd–Cl CN linearly increases at the higher ratios to 2 and 1.6 for the A11- and A6,11-capped structures, respectively, at the maximum Pd/peptide ratio of 4. This suggests that, for these materials, a degree of Cl coordination to the particle surface is present from Cl^- ions in solution in addition to the peptide that gives rise to the observed Pd–O/N coordination.

Upon characterization of the peptide-capped Pd nanoparticles, their catalytic activity was studied for the Stille coupling of 4-iodobenzoic acid with $PhSnCl_3$ to prepare biphenylcarboxylic acid (BPCA), which is illustrated in Figure 6a. Studies of the catalytic functionality are proving to be an important method to characterize the biological/inorganic surface of nanomaterials, as the reactivity is dependent upon the surface structure and composition. To characterize the reactivity of the materials, the turnover frequency (TOF) values for the individual reactions for all of the nanoparticles prepared were determined over the course of 1.00 h and are presented in Figure 6b. A general decrease is observed in catalytic activity as the Pd/peptide ratio is decreased; however, the total Pd loading for each reaction remains constant at

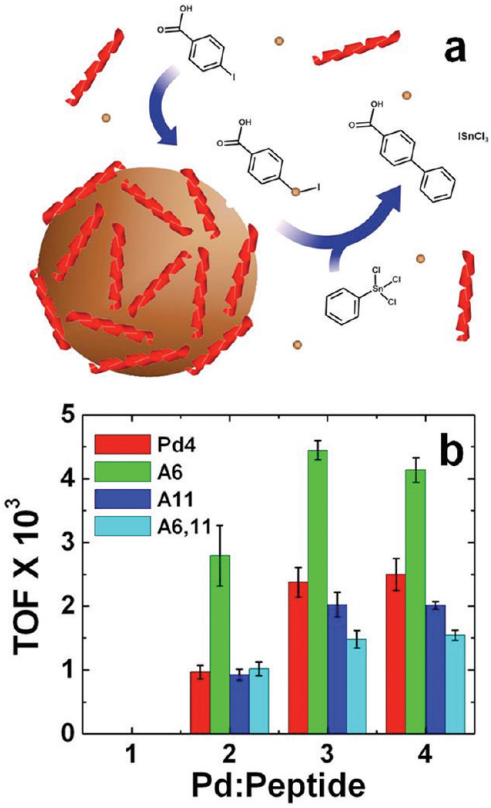

Figure 6. Catalytic analysis of the peptide-capped Pd nanoparticles. (a) Proposed leaching mechanism of Stille coupling employing the materials, and (b) TOF analysis for the nanoparticles as a function of peptide surface and Pd/peptide ratio used to fabricate the particles.

0.050 mol %. The particles prepared with the Pd4 peptide at a Pd/peptide ratio of 4 demonstrated a TOF value of 2496 ± 252 mol BPCA (mol Pd $\times$ h)$^{-1}$.[9] At this same ratio, the A6-capped Pd particles showed an almost 2-fold increase in catalytic activity, with a TOF of 4314 ± 190 mol BPCA (mol Pd $\times$ h)$^{-1}$. The A11-based materials demonstrated catalytic activity that was diminished as compared to the Pd4-capped materials with a TOF value of 2010 ± 59 mol BPCA (mol Pd $\times$ h)$^{-1}$, while the A6,11-prepared Pd nanoparticles had the lowest activity with a TOF of 1565 ± 66 mol BPCA (mol Pd $\times$ h)$^{-1}$.

When using the materials prepared at a Pd/peptide ratio of 3, little deviation in the catalytic activity for these structures was noted as compared to the nanoparticles prepared at a ratio of 4; however, at subsequently lower ratios, diminished reactivity was observed. For the 2:1 ratio previously presented for the Pd4-based materials,[9] the particles showed a drop in reactivity with a TOF value of 965 ± 105 mol BPCA (mol Pd $\times$ h)$^{-1}$ as compared to the materials prepared at higher ratios. This same loss in activity was observed for the A6-prepared particles where a minimized TOF of 2793 ± 473 mol BPCA (mol Pd $\times$ h)$^{-1}$ was observed. For the A11- and A6,11-capped materials, diminished TOF values of 1026 ± 191 and 1009 ± 78 mol BPCA (mol Pd $\times$ h)$^{-1}$, respectively, were observed.

Interestingly, at this ratio, even though minimized reactivity is evident for all of the materials, the A6-capped particles still remain significantly more catalytically active as compared to the particles generated with the other peptides. Finally, for the materials prepared at a Pd/peptide ratio of 1, no activity was observed for any of the particles over the time frame of the TOF study.

The catalytic results, in combination with the high-resolution characterization of the materials, afford the ability to infer unique structural information concerning the biotic/abiotic interface of the peptide-capped Pd nanomaterials. First, from the UV−vis and TEM evidence, it is clear that the peptides are able to cap the Pd structures where particles of the same size are generated using the same peptide, regardless of the Pd/peptide ratio employed during materials synthesis. Furthermore, by slight modifications to the sequence, changes in the particle size are possible over the very small size range of 1.8−3.0 nm in diameter. The changes to the peptide sequence are likely to alter its recognition for the nanoparticle surface, which thereby alters the binding strength to change the particle size. We have previously established using the Pd4 sequence that the peptide is able to recognize and bind the face-centered cubic (fcc) structure of Pd,[9] which is likely embedded during the phage display process. By altering the specific binding motif, which has been previously suggested to arise from the two histidine residues,[22] this likely alters the recognition element of the sequence to result in the larger particle sizes. Furthermore, CD and QCM data directly show that stronger binding sequences present more significantly altered secondary structures when bound to the particle surface as compared to free in solution, further suggesting that modifications to the sequences alters the recognition ability and binding strength of the peptides for Pd. This would give rise to the larger structures and different selected sizes for the A6-, A11-, and A6,11-capped Pd nanoparticles. The results also suggest that binding of the histidine at the 11 position is required for increased specificity and binding strength due to the smaller particles prepared using the native Pd4 and A6 sequences as compared to the A11 and A6,11 peptides that remove binding at this site.

The argument concerning the importance of binding at the 11 position in the peptide sequence is further strengthened in light of the catalytic results. When comparing the TOF values for the materials prepared at the same Pd/peptide ratio, it is evident that reactivity of the peptide-capped particles is altered as a function of the peptide on the surface following the trend of A6 > Pd4 > A11 > A6,11. For those peptides that modified binding at the 11 position, significantly reduced activity is noted. Additionally, upon the basis of the EXAFS analysis of the reduced particles, the A11- and A6,11-capped structures prepared at ratios of 3 and 4 possess a substantial amount of Cl^- coordination at the nanoparticle surface, which likely affects the functionality by inhibiting reactivity at these sites, leading to the decreased TOF values. For this reaction, the materials likely follow a Pd atom leaching process,[12] consistent with other C−C coupling schemes;[30] therefore, the changes in particle size observed here are not anticipated to alter the reactivity.[31] As a result, the variations in reactivity can be directly attributed to the particle surface structure that is controlled by the peptides. Furthermore, while particles of nearly identical size and structure are prepared at all of the ratios for the different peptide sequences, the catalytic activity of the materials decreases for those particles prepared at lower ratios. For the Pd4-based materials, this has been rationalized to be a function of the degree of reduction where decreased reduction at the lower ratio materials leads to diminished reactivity.[9] For the A6-, A11-, and A6,11-capped particles, similar degrees of reduction are observed across the different particles prepared, thus the same amount of reduced Pd metal in each reaction is roughly equivalent. This indicates that additional effects are likely to contribute to the lowering of reactivity for particles prepared at the lower ratios. To that end, the main difference between the sets of materials is the amount of free peptide in the reactions at the lower ratios. In the higher ratios (3 and 4), all of the peptide is anticipated to be coordinated to the Pd particle surface to ensure colloidal stability. When insufficient peptide is present, Pd black precipitation is anticipated, which occurs for materials at ratios >4, thus suggesting complete particle capping by the peptides at lower ratios. At the lowest ratios (1 and 2), excess peptide is present in the reaction to cap the particle surface, thus metal-free sequences are present in solution that are transferred to the reaction. Due to the Pd leaching process of nanoparticle-driven Stille coupling,[12] free Pd atoms are released once the BPCA product is generated. In this sense, the free peptide could then strongly bind these Pd atoms, thus sequestering them from solution to lead to the lower TOF values. This illustrates multiple effects that are otherwise overlooked with respect to nanoparticle concentrations and material/passivant relationships. Following this approach, more free peptide in solution would lead to diminished reactivity, which is indeed observed as the reactions are processed using the materials generated at lower Pd/peptide ratios. Taken together, this suggests that three effects, the biotic/abiotic surface structure, the degree of Pd reduction, and the amount of free peptide in solution, contribute to the observed reactivity.

To test the effect of free peptide on the reactivity, the following control was studied. First, one batch of Pd nanoparticles was generated using the Pd4 sequence prepared at a Pd/peptide ratio of 4, which was then

split into two equal volumes. To one of the Pd nanoparticle samples was added sufficient excess Pd4 peptide such that the Pd/peptide ratio was decreased to 1, while in the second sample, no additional peptide was added, thus the Pd/peptide ratio remained at 4. Next, two Stille coupling reactions were prepared that were catalytically driven by the nanoparticle samples that modulated the Pd/peptide ratio. As a result, the reaction catalyzed by particles with a Pd/peptide ratio of 4 proceeded as normal with a TOF value consistent with the observations of Figure 6b; however, the second reaction with excess peptide failed to produce a quantifiable amount of product in the 1.00 h TOF time frame. This suggests that the excess peptide in solution does indeed alter the reactivity, which could arise from binding of leached Pd atoms generated during the catalytic cycle.

These results directly relate to the sequences determined *via* phage display. While the Pd4 peptide was isolated with affinity for Pd, additional sequences were designed that possessed similar binding abilities. By changing the peptide sequence, however, the degree of affinity can be modulated to control particle size and functionality. In some instances, this can decrease the activity; however, selected modifications can be used to substantially increase the functionality, which is highly desirable. This suggests that while phage display can be used to isolate sequences that bind a target substrate, the technique may not elucidate the optimal sequence to control both material structure *and* activity. These two considerations are likely a function of the binding strength, surface peptide/particle structure, and inorganic composition, which could be tuned by the peptide sequence. The peptides isolated *via* phage display are likely to be optimized for the strongest binding sequences; however, many applications, including catalysis, are enhanced by ligands that are more loosely bound to allow substrate interactions with the metallic surface. Furthermore, only a limited subset of the total number of dodecamer peptides possible is present in the phage library, thus limiting the number sequences that could be isolated. Taken together, these results suggest that while phage display is an excellent technique to elucidate peptides with specific affinity, the sequences that are determined may not be optimal for the final material application. By employing selective peptide modifications, new sequences can be rationally designed to control the structure, properties, and function of the final materials.

CONCLUSIONS

In conclusion, these results suggest that simple changes in peptide sequences can control the size and functionality of nanoparticles by modulating peptide surface binding capabilities. By changing just a single amino acid, selectable particle sizes can be achieved that vary over a small size range (2−3 nm), producing nearly monodisperse, single-crystal nanoparticles. This size selectivity likely arises by modulating the binding motif of the peptide to the target materials, thus resulting in changes to the biotic/abiotic region of peptide-capped nanoparticles that possesses significant effects on the functionality of the materials. Taken together, these results suggest that peptides may be unique ligands to allow for selective nanoparticle fabrication schemes with exacting control over the size, shape, composition, crystallinity, and functionality of nanomaterials. Further results are required to confirm such capabilities, which are presently underway.

MATERIALS AND METHODS

Chemicals. FMOC-protected amino acids, WANG resins modified with the initial FMOC-protected amino acid of the sequence, piperidine, diisopropyl ethylamine, HBTU, and HOBt were purchased from Advanced ChemTech (Louisville, KY). Trifluoroacetic acid, 4-iodobenzoic acid, sodium sulfate, 4-*t*-butylphenol, and deuterated chloroform were all purchased from Fisher Scientific (Pittsburgh, PA). $PhSnCl_3$, triisopropylsilane, triisopropylsilane, potassium tetrachloropalladate, and potassium hydroxide were acquired from Sigma Aldrich (Milwaukee, WI). Diethyl ether, *N*,*N*-dimethylformamide, methanol, and acetonitrile were purchased from Pharmco AAPER (Shelbyville, KY), while $NaBH_4$ was obtained from EMD Chemicals (Gibbstown, NJ). All reagents were used as received. Milli-Q water (18 MΩ·cm; Millipore, Bedford, MA) was used for all aqueous experiments.

Nanoparticle Synthesis. Peptide synthesis, purification, and confirmation were conducted using standard methods.[25] Four different sets of nanoparticles were then prepared that varied the Pd/peptide ratio using the peptides of the designed library (Table 1). Here, the production of nanoparticles using a ratio of 4 is described; however, identical methods were employed to prepare materials at lower Pd/peptide ratios using a lower concentration of K_2PdCl_4. A peptide stock solution was prepared at a concentration of 10 mg/mL in water. Next, 100 μL of the peptide stock was diluted in 4.775 mL of water, where the final peptide reaction concentration was 150 μM. To this solution was added 31.25 μL of a freshly prepared 100 mM K_2PdCl_4 solution, and the mixture was stirred for 30.0 min to allow for Pd^{2+}/peptide complexation to reach completion. Next, 100 μL of a 100 mM $NaBH_4$ solution, freshly prepared in water, was added to reduce the materials, which resulted in an immediate solution color change from pale yellow to brown. The reaction was allowed to stand for 1.00 h to ensure complete Pd^{2+} reduction.

Stille Reaction. As a model catalytic analysis, the Stille coupling of 4-iodobenzoic acid with $PhSnCl_3$ to produce BPCA was used following standard procedures.[11] Stille couplings were set up for each nanoparticle sample prepared with the four different peptides at the selected Pd/peptide ratios. For each reaction, 4-iodobenzoic acid (310 mg) was dissolved in 20.0 mL of 2.25 M aqueous KOH. This solution was stirred vigorously for ∼30.0 min to ensure dissolution. To this stirred solution, 246 μL of $PhSnCl_3$ was added and allowed to dissolve, after which a sufficient volume of Pd nanoparticles was added to reach a Pd

loading of 0.05 mol %. Since the Pd concentration varies in the different materials syntheses based upon the Pd/peptide ratio, different volumes of nanoparticles are required, with water added to the reactions such that the final volume is constant for all ratios. Immediately upon nanoparticle addition to the Stille reaction, a 2.00 mL aliquot was extracted, followed by subsequent aliquots removed at selected time points over 1.00 h. Upon collection, the aliquots were quenched with 12.5 mL of 5.00% aqueous HCl. Each sample was then extracted with three 20.0 mL volumes of ether and washed twice with brine. Then, 75.0 mg of 4-*t*-butyl phenol was added to the ether layer as an internal standard for analysis of reaction progress. The ether solvent was then removed using a Büchi Rotovapor R-210. Finally, 1−2 mg of the dry powder was dissolved in 1.00 mL of deuterated chloroform and then analyzed by ^{1}H NMR to determine the TOF of the reaction.[11]

Characterization. UV−vis analysis of the materials was completed using an Agilent 8453 photodiode array spectrometer employing 0.2 cm path length quartz cuvettes. Pd^{2+}/peptide ratio samples in water (ratios ranging from 1 to 10) were analyzed using a peptide solution at the reaction concentration as the blank. UV−vis analysis of the nanoparticles prepared after reduction from these samples was completed using identical methods. TEM analysis was conducted using a JEOL 2010F TEM operating at 200 kV. Individual samples were prepared on 400 mesh Cu grids coated with an ultrathin layer of carbon (EM Sciences; Hatfield, PA). A small sample of each solution (5.00 μL) was deposited on the surface of the grid and allowed to dry overnight. Analysis of >100 nanoparticles observed at different regions of the grid was used to determine particle size distributions. XAFS analysis of the materials was completed using previously described methods.[9] Briefly, Pd *K*-edge XAFS studies were performed at the X18B beamline at the National Synchrotron Light Source at Brookhaven National Laboratory. All samples, both unreduced Pd^{2+}/peptide complex and reduced Pd nanoparticles, were dried *via* lyophilization to form a powder. The powders were then uniformly spread on adhesive tape, and their X-ray absorption coefficient was measured in transmission mode between 150 eV below and 1350 eV above the Pd *K*-edge (24353 eV). The Artemis program from the IFEFFIT XAFS analysis software suite was used to analyze the EXAFS data by fitting theoretical contributions to the experimental spectrum.[26] The theoretical signal was obtained using FEFF6 code that calculates photoelectron scattering amplitudes and phases for a given atomic configuration. In the fits, the amplitude factor (S_0^2 = 0.885) was added, which was obtained from analysis of Pd foil. Also added are coordination numbers of nearest neighbors to Pd, their distances, and mean square disorders (σ^2) in those distances. In addition, we varied the photoelectron energy origin corrections for different contributions, as described in greater detail below. To construct theoretical contributions for Pd−O/N, we used a reference crystal structure of PdO. To construct Pd−Cl, we used the structure of K_2PdCl_4, and to construct Pd−Pd theory, we used the structure of bulk Pd. These contributions, each carrying its own energy origin correction (since they were obtained from different structures), were combined in Artemis into the total theoretical signal. The data from all reduced and complexed species were processed using this modeling strategy.

CD spectra were obtained on a Jasco J-815 CD spectrometer using a quartz cuvette. Peptides were dissolved in double deionized water with varying amounts of Pd^{2+} (6.25, 12.5, 18.75, and 25.0 μL) to reach desired Pd^{2+}/peptide ratio and diluted to a peptide concentration of 16 μM in water for CD measurements. Nanoparticles were prepared at equivalent ratios and likewise diluted for CD. The CDPro software package was used for analysis of CD spectra to deconvolute secondary structure contributions. QCM measurements were performed using a Q-Sense E4 QCM-D system with standard flow modules. Pd surfaces were prepared by sputter-coating 200 Å of Pd onto an Au QCM sensor (QSX301). The surfaces were cleaned by heating in a solution of 5:1:1 water, 25% ammonia, and 30% hydrogen peroxide followed by extensive rinsing with water and 99% ethanol. The peptides were dissolved in double deionized water at a concentration of 10 μg/mL and flowed across QCM sensors at a rate of 0.17 mL/min. The third overtone frequency was monitored for adsorption measurements.

Conflict of Interest: The authors declare no competing financial interest.

Acknowledgment. This material is based upon work supported by the National Science Foundation under Grant No. CBET-1157431(M.K.) and by the Air Office of Scientific Research (R.N.). A.I.F. acknowledges support by U.S. Department of Energy Grant DE-FG02-03ER15476. Beamline X18B at the NSLS is supported in part by the Synchrotron Catalysis Consortium, U.S. Department of Energy Grant No. DE-FG02-05ER15688. M.K. further acknowledges support from the University of Miami. R.C. acknowledges student fellowship support from the Research Challenge Trust Fund. The authors are grateful to Dr. R. Vasic for help with XAFS measurements.

Supporting Information Available: UV−vis analysis of the materials, digital images of the reduced particle solutions, comparison of particle sizes, CD data analysis tables, QCM analysis of peptide binding, and EXAFS fits to theoretical models. This material is available free of charge *via* the Internet at http://pubs.acs.org.

REFERENCES AND NOTES

1. Sarikaya, M.; Tamerler, C.; Jen, A. K.-Y.; Schulten, K.; Baneyx, F. Molecular Biomimetics: Nanotechnology through Biology. *Nat. Mater.* **2003**, *2*, 577–585.
2. Mann, S. *Biomineralization: Principals and Concepts in Bioinorganic Materials Chemistry*; Oxford University Press: New York, 2002.
3. Round, F. E.; Crawford, R. M.; Mann, D. G. *Magnetite Biomineralization and Magnetoreception in Organisms*; Plenum Press: New York, 1985.
4. Round, F. E.; Crawford, R. M.; Mann, D. G. *The Diatoms: Biology & Morphology of the Genera*; Cambridge University Press: Cambridge, 1990.
5. Lee, Y. J.; Yi, H.; Kim, W.-J.; Kang, K.; Yun, D. S.; Strano, M. S.; Ceder, G.; Belcher, A. M. Fabricating Genetically Engineered High-Power Lithium Ion Batteries Using Multiple Virus Genes. *Science* **2009**, *324*, 1051–1055.
6. Nam, K. T.; Kim, D.-W.; Yoo, P. J.; Chiang, C.-Y.; Meethong, N.; Hammond, P. T.; Chiang, Y.-M.; Belcher, A. M. Virus-Enabled Synthesis and Assembly of Nanowires for Lithium Ion Battery Electrodes. *Science* **2006**, *312*, 885–888.
7. Bhandari, R.; Knecht, M. R. Effects of the Material Structure on the Catalytic Activity of Peptide-Templated Pd Nanomaterials. *ACS Catal.* **2011**, *1*, 89–98.
8. Jakhmola, A.; Bhandari, R.; Pacardo, D. B.; Knecht, M. R. Peptide Template Effects for the Synthesis and Catalytic Application of Pd Nanoparticle Networks. *J. Mater. Chem.* **2010**, *20*, 1522–1531.
9. Coppage, R.; Slocik, J. M.; Briggs, B. D.; Frenkel, A. I.; Heinz, H.; Naik, R. R.; Knecht, M. R. Crystallographic Recognition Controls Peptide Binding for Bio-Based Nanomaterials. *J. Am. Chem. Soc.* **2011**, *133*, 12346–12349.
10. Coppage, R.; Slocik, J. M.; Sethi, M.; Pacardo, D. B.; Naik, R. R.; Knecht, M. R. Elucidation of Peptide Effects that Control the Activity of Nanoparticles. *Angew. Chem., Int. Ed.* **2010**, *49*, 3767–3770.
11. Pacardo, D. B.; Sethi, M.; Jones, S. E.; Naik, R. R.; Knecht, M. R. Biomimetic Synthesis of Pd Nanocatalysts for the Stille Coupling Reaction. *ACS Nano* **2009**, *3*, 1288–1296.
12. Pacardo, D. B.; Slocik, J. M.; Kirk, K. C.; Naik, R. R.; Knecht, M. R. Interrogating the Catalytic Mechanism of Stille Coupling Reactions Employing Bio-Inspired Pd Nanoparticle Catalysts. *Nanoscale* **2011**, *3*, 2194–2201.
13. Slocik, J. M.; Naik, R. R. Biologically Programmed Synthesis of Bimetallic Nanostructures. *Adv. Mater.* **2006**, *18*, 1988–1992.
14. Kuang, Z.; Kim, S. N.; Crookes-Goodson, W. J.; Farmer, B. L.; Naik, R. R. Biomimetic Chemosensor: Designing Peptide Recognition Elements for Surface Functionalization of Carbon Nanotube Field Effect Transistors. *ACS Nano* **2010**, *4*, 452–458.

15. Slocik, J. M.; Zabinsky, J. S.; Phillips, D. M.; Naik, R. R. Colorimetric Response of Peptide-Functionalized Gold Nanoparticles to Metal Ions. *Small* **2008**, *4*, 548–551.
16. Kim, S. N.; Slocik, J. M.; Naik, R. R. Strategy for the Assembly of Carbon Nanotube-Metal Nanoparticle Hybrids Using Biointerfaces. *Small* **2010**, *6*, 1992–1995.
17. Chen, C.-L.; Rosi, N. L. Preparation of Unique 1-D Nanoparticle Superstructures and Tailoring Their Structural Features. *J. Am. Chem. Soc.* **2010**, *132*, 6902–6903.
18. Chen, C.-L.; Zhang, P.; Rosi, N. L. A New Peptide-Based Method for the Design and Synthesis of Nanoparticle Superstructures: Construction of Highly Ordered Gold Nanoparticle Double Helices. *J. Am. Chem. Soc.* **2008**, *130*, 13555–13557.
19. Kim, S. N.; Kuang, Z.; Slocik, J. M.; Jones, S. E.; Cui, Y.; Farmer, B. L.; McAlpine, M. C.; Naik, R. R. Preferential Binding of Peptides to Graphene Edges and Planes. *J. Am. Chem. Soc.* **2011**, *133*, 14480–14483.
20. Dickerson, M. B.; Sandhage, K. H.; Naik, R. R. Protein- and Peptide-Directed Syntheses of Inorganic Materials. *Chem. Rev.* **2008**, *108*, 4935–4978.
21. Heinz, H.; Farmer, B. L.; Pandey, R. B.; Slocik, J. M.; Patnaik, S. S.; Pachter, R.; Naik, R. R. Nature of Molecular Interactions of Peptides with Gold, Palladium, and Pd−Au Bimetal Surfaces in Aqueous Solutions. *J. Am. Chem. Soc.* **2009**, *131*, 9704–9714.
22. Pandey, R. B.; Heinz, H.; Feng, J.; Farmer, B. L.; Slocik, J. M.; Drummy, L. F.; Naik, R. R. Adsorption of Peptides (A3, Flg, Pd2, Pd4) on Gold and Palladium Surfaces by a Coarse-Grained Monte Carlo Simulation. *Phys. Chem. Chem. Phys.* **2009**, *11*, 1989–2001.
23. Tomásio, S. M.; Walsh, T. R. Modeling the Binding Affinity of Peptides for Graphitic Surfaces. Influences of Aromatic Content and Interfacial Shape. *J. Phys. Chem. C* **2009**, *113*, 8778–8785.
24. Yu, J.; Becker, M. L.; Carri, G. A. A Molecular Dynamics Simulation of the Stability-Limited Growth Mechanism of Peptide-Mediated Gold-Nanoparticle Synthesis. *Small* **2010**, *6*, 2242–2245.
25. Chan, W. C.; White, P. D. *Fmoc Solid Phase Peptide Synthesis: A Practical Approach*; Oxford University Press: New York, 2000.
26. Newville, M. IFEFFIT: Interactive XAFS Analysis and FEFF Fitting. *J. Synchrotron Radiat.* **2001**, *8*, 322–324.
27. Scott, R. W. J.; Ye, H.; Henriquez, R. R.; Crooks, R. M. Synthesis, Characterization, and Stability of Dendrimer-Encapsulated Palladium Nanoparticles. *Chem. Mater.* **2003**, *15*, 3873–3878.
28. Skoog, D. A.; West, D. M.; Holler, F. J.; Crouch, S. R. *Fundamentals of Analytical Chemistry* 8th ed.; Brooks Cole: New York, 2003.
29. Frenkel, A. I.; Hills, C. W.; Nuzzo, R. G. A View from the Inside: Complexity in the Atomic Scale Ordering of Supported Metal Nanoparticles. *J. Phys. Chem. B* **2001**, *105*, 12689–12703.
30. Astruc, D. Palladium Nanoparticles as Efficient Green Homogeneous and Heterogeneous Carbon−Carbon Coupling Precatalysts: A Unifying View. *Inorg. Chem.* **2007**, *46*, 1884–1894.
31. Diallo, A. K.; Ornelas, C.; Salmon, L.; Aranzaes, J. R.; Astruc, D. "Homeopathic" Catalytic Activity and Atom-Leaching Mechanism in Miyaura−Suzuki Reactions under Ambient Conditions with Precise Dendrimer-Stabilized Pd Nanoparticles. *Angew. Chem., Int. Ed.* **2007**, *46*, 8644–8648.